

# Multi-Layer Ultrasonic Imaging of As-Built Wire + Arc Additive Manufactured Components

Rastislav Zimmermann<sup>1</sup>, Ehsan Mohseni<sup>1</sup>, David Lines<sup>1</sup>, Randika K. W. Vithanage<sup>1</sup>, Charles N. MacLeod<sup>1</sup>, Stephen G. Pierce<sup>1</sup>, Anthony Gachagan<sup>1</sup>, Yashar Javadi<sup>1</sup>, Stewart Williams<sup>2</sup>, Jialou Ding<sup>2</sup>

<sup>1</sup>Centre for Ultrasonic Engineering, University of Strathclyde, Glasgow, UK

<sup>2</sup> Welding Engineering and Laser Processing Centre, University of Cranfield, Cranfield, UK

**Corresponding Author:** Rastislav Zimmermann, rastislav.zimmermann@strath.ac.uk,  
Centre for Ultrasonic Engineering, Department of Electronic & Electrical Engineering, University of Strathclyde, 204 George Street, Glasgow, G1 1XW, United Kingdom

## Abstract

Non-Destructive Evaluation (NDE) of metal Additively Manufactured (AM) components is crucial for the identification of any potential defects. Ultrasonic testing is recognised for its volumetric imaging capability in metallic components and high defect sensitivity. However, conventional ultrasonic techniques suffer from challenges when deployed on components with curved and non-planar geometries, such as those often encountered in AM builds.

The body of work introduces the concept of inspection of Wire+Arc Additive Manufacture (WAAM) components from their non-planar as-built surface, eliminating the requirement for post-manufacturing machining. In-situ or post-manufacturing inspection is enabled via an autonomously deployed conformable phased array roller-probe deploying Synthetic Aperture Focusing Technique (SAFT)-surface finding and multi-layer adaptive Total Focusing Method (TFM) algorithms, for fully focussed imaging of the as-built WAAM component.

The concept of the imaging approach is demonstrated by inspection, through the as-built surface, of two titanium WAAM components, one containing reference bottom-drilled holes, and the other with intentionally introduced Lack of Fusion (LoF) defects.

The TFM images of the WAAM components feature sufficient Signal-to-Noise Ratio to enable defect detection along with strong agreement against reference X-Ray CT data, confirming the competency of the approach for volumetric or layer-specific inspection of as-built WAAM components.

**Keywords:** Ultrasound inspection of additive manufacturing, ultrasound array imaging, Adaptive Total Focusing Method (ATFM), Full Matrix Capture (FMC), Synthetic Aperture Focusing Technique (SAFT), Wire + Arc Additive Manufacture (WAAM),

This is a peer-reviewed, accepted author manuscript of the following article: Zimmermann, R., Mohseni, E., Lines, D., Vithanage, R. K. W., MacLeod, C. N., Pierce, S. G., Gachagan, A., Javadi, Y., Williams, S., & Ding, J. (2021). Multi-layer ultrasonic imaging of as-built Wire + Arc additive manufactured components. *Additive Manufacturing*, 48(Part A ), [102398]. <https://doi.org/10.1016/j.addma.2021.102398>

43

# 1. Introduction

## 1.1: Additive Manufacturing

45 Additive Manufacturing (AM) is a process of joining materials layer upon layer to produce components  
46 from 3D model data [1]. AM is a substitute for traditional manufacturing methods, in which, the components are  
47 commonly subtracted by milling processes or formed in molds [2]. In AM of metals, a powder or wire feedstock  
48 is melted by an energy source. Powder bed fusion processes such as laser beam melting, or electron beam melting  
49 are used to build components in closed chambers by fusing the powder to create a layer of the final structure. The  
50 bed on which the layer is deposited is then lowered and the process is repeated until the full component is com-  
51 pleted. The key advantage of such a process is the high geometric accuracy of the final component however, the  
52 process is traditionally slow; hence, the components produced are typically small [3]. Large scale application of  
53 additive manufacturing is commonly associated with directed energy deposition processes, such as laser metal  
54 deposition or Wire+Arc Additive Manufacturing (WAAM), where a wire or powder is fed into the melt pool  
55 created by laser, electron beam or an electric arc. The dimensional accuracy of these processes is commonly traded  
56 against the increased size of the final component and the deposition speed [2].

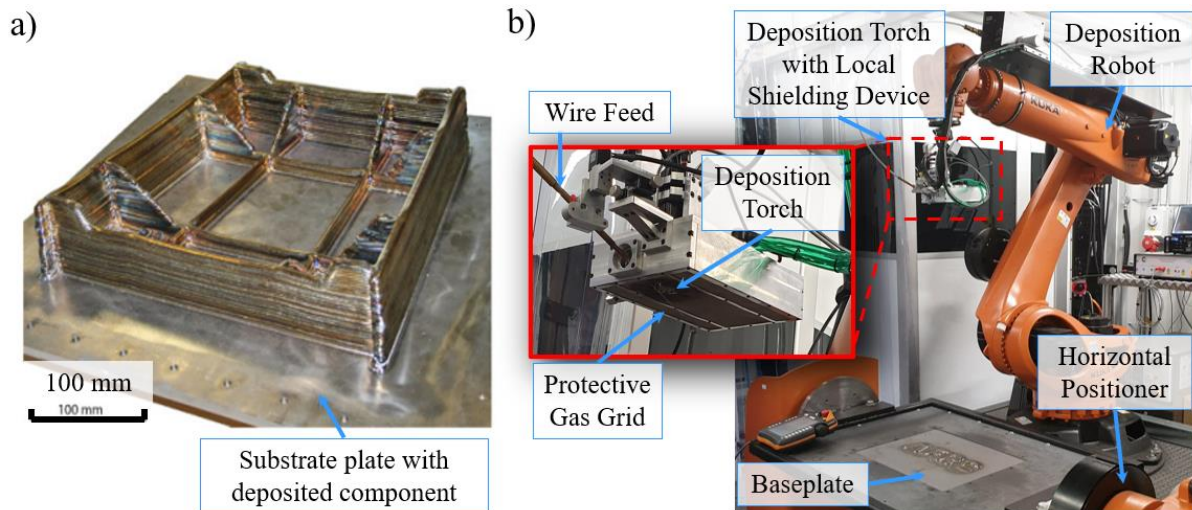
## 1.2: Wire + Arc Additive Manufacturing (WAAM)

58 Industrial sectors such as aerospace, defence and energy have shown a growing interest in the capability of  
59 WAAM, as the process offers the potential for manufacturing cost-effectiveness owing to reduced material waste,  
60 decreased production time and increased design flexibility when producing large and complex components as  
61 shown on Figure 1 (a) [4]. For instance, the authors have reported material savings of approximately 220 kg in  
62 manufacturing of a 24 kg titanium Ti-6AL-4V (Ti-64) landing gear assembly with a deposition rate of 0.8kg/hour.  
63 [4]. In this example, the component consisted of complex features such as tiled walls and T-junctions, proving the  
64 process as a suitable replacement for traditional subtractive techniques where machining and waste make the  
65 process inefficient. [5]. The titanium alloy utilized is extensively used in aerospace and chemical engineering  
66 because of its good fracture toughness, high strength and corrosion resistance. [6].

67 WAAM components are typically deposited robotically using an electric arc, acting as a heat source, along  
68 with wire feedstock in a similar fashion to welding, as illustrated in Figure 1(b) [4, 7]. The component geometry  
69 is commonly a series of deposited walls with parallel or single oscillating beads. [8]. When depositing materials  
70 that could suffer from oxidation and subsequently have induced defects during deposition, additional shielding is  
71 required. In [8], WAAM deposition of large titanium components was enabled through the deployment of a local  
72 shielding device (Fig 1 (b)) which supplies the build area with shielding gas, such as argon or helium and reducing  
73 the potential for contamination. Additional methods of shielding WAAM deposition utilize tent-like structures,  
74 fully enclosing the deposition apparatus and filled with shielding gas to reduce the components contact with oxy-  
75 gen to a minimum. [9].

76 Although the shielding system protects the molten pool from oxidation, reducing the potential for porosity  
77 and inclusions, similar to many welding or manufacturing processes, Lack of Fusion (LoF) and keyholes defects  
78 may occur in the components affecting their structural integrity and fitness for service. [10]. These undesired  
79 deposition defects in safety-critical WAAM components predominantly originate from the poor quality of the  
80 wire, incorrect definition of the process parameters and contamination introduced by the environment. [4]. There-  
81 fore, it is essential to assess the quality and integrity of manufactured components through Non-Destructive Eval-  
82 uation (NDE) before they can be certified and enter their intended service application.

83



84

85 **Figure 1** (a) WAAM landing gear rib component, and (b) WAAM robotic deposition setup [4]86 *1.3: Inspection of Additive Manufactured Components*87 NDE is a process for evaluating the structural integrity and characteristics of a component without affecting  
88 the useful serviceability of the part.89 X-ray imaging techniques such as radiography have already been successfully utilized and evaluated on AM  
90 components, detecting porosity, inclusions and lack of fusion defects in fully-built WAAM components [11]. In  
91 X-ray testing, radiation energy is sent through the component and captured by an analog or digital photosensitive  
92 reception medium to form an image showing inconsistencies of the penetrated energy caused by volumetric dis-  
93 continuities. However, the application of this technique is generally time taking, hazardous and expensive [12].94 More advanced techniques such as X-ray Computed Tomography (XCT), have also been utilized on AM  
95 components. In XCT, normally a series of X-ray images are taken from different angles surrounding an object,  
96 and then, the 3D model of the component is constructed via computing the amount of X-ray exposure of consti-  
97 tuent cubic elements of the 3D volume [13]. The technique shows sensitivity to detect and characterize defects  
98 deep within AM components, without the need for surface preparation and has been demonstrated of detecting  
99 defects as small as 600 $\mu$ m in titanium components produced using electron beam techniques [14]. The downside  
100 of this technique is, however, the costs associated with the equipment and analysis station, and the impracticality  
101 of in-situ inspection of large components [15].102 Regarding the application of electromagnetic-based inspection techniques, Eddy Current Testing (ECT) is a  
103 technique where circular currents are generated in a conductive material by a coil connected to a current generator  
104 and where a defect is highlighted by perturbations in the current [16]. ECT with customized spatially design coils,  
105 with a shape matched to the as-built curved surface of a WAAM component, were shown to be capable of detect-  
106 ing side-drilled holes of 0.35 mm at depths of 2 mm in aluminum samples [17]. Even though ECT offers very  
107 high surface/near-surface sensitivity and detectability, the penetration depth is traditionally limited to a few mil-  
108 limeters below the surface depending on the coil design, test frequency, and material properties [16]. Therefore,  
109 while it offers the potential for on-line screening of newly deposited upper layers during the manufacturing process  
110 [11], it is not best-suited for deeper volumetric inspection of WAAM components and multi-layers, or the in-  
111 process inspection of preceding layers for defects such as delayed cracking [18, 19].112 Among other NDE methods deployed for the AM inspection, thermography has also shown promise when  
113 used within the deposition cell and with a safe distance from the heat source to monitor the defect formation  
114 during the process allowing for possible in-situ repair [14]. During the thermography tests, the variations of the  
115 thermal gradient indicating the flaws were monitored in the AM components. The downside of this technique is,  
116 however, the lower sensitivity in-depth and due to surface roughness alongside the time required to induce the  
117 required heat in the sample [20].118 Conventional Ultrasound Testing (UT) or modern phased array technology is often the preferred inspection  
119 technique for volumetric examination of metallic welded components [21]. This inspection method offers high  
120 sensitivity to small defects and is capable of pinpointing, characterizing and sizing different shapes and

121 orientations [22]. Additionally, considering the advances in phased array technology, signal processing and ro-  
122 botics, the technique is feasible to integrate within automated robotic systems for the inspection of welds and AM  
123 components efficiently and safely [23, 24]. Typically, in weld inspection, angled wedges mounted alongside the  
124 joint on the parent material, are normally required to guide the wave towards the weld at a certain defined angle  
125 or the emerging use of novel conformable liquid-filled delay lines allow inspection directly on top of the fully  
126 filled weld cap [24].

127 Laser ultrasound, as another mechanical method of generating ultrasonic waves, is a non-contact method  
128 capable of detecting defects as small as 0.2mm in diameter in AM components and has shown potential for on-  
129 line monitoring [25]. The method has been deployed to detect subsurface defects of AM components produced  
130 using laser powder bed fusion [25] and on WAAM components detecting surface cracks, flat bottom holes and  
131 through holes [26]. However, laser ultrasonic setups have historically featured very high initial costs, slow gener-  
132 ation, acquisition and data processing times, while also being sensitive to surface finish [27] and safety consider-  
133 ations.

134 Lastly, the deployment of gas or air-coupled UT is inherently limited by the large acoustic impedance mis-  
135 match between the air and solid inspection medium, resulting in a large loss of energy ( $< 140$  dB) and hence  
136 sensitivity, therefore not endearing this method for the inspection of AM components [28].

137 Considering the capabilities of NDE techniques previously trialed on AM components and summarized  
138 above, ultrasonic techniques offer strong potential for in-situ as-built WAAM volumetric inspection. However,  
139 challenges remain related to suitable coupling between the ultrasound probe and the as-built WAAM surface,  
140 along with imaging of the component through the irregular as-built surface.

#### 141 *1.4: In-Situ Inspection of As-Built WAAM Components*

142 Traditionally, WAAM component manufacturing and NDE tend to be conducted separately and sequentially  
143 within the build process. Merging both these processes by incorporating the NDE within the manufacturing cell  
144 aims to save time and costs associated with part relocation and transfer between the cells [24]. In current ultrasonic  
145 inspection practices, completed AM components are either: (a) scanned inside immersion tanks using gantry sys-  
146 tems, or (b) manually tested after their surface is machined flat for contact ultrasonic inspection [29-32] [33, 34].  
147 However, immersion testing of large-scale WAAM components is very challenging and sometimes impractical,  
148 and even in such a configuration, a flat machined surface is preferred to avoid the ultrasonic wave refracting and  
149 scattering at the surface/couplant interface. Moreover, to conduct the immersion test, the component is often  
150 transferred to another cell prolonging the full build process significantly.

151 For conventional ultrasonic testing to be performed on a WAAM component, often a milling operation must  
152 be introduced into the production cycle [35], again to avoid wave refraction and scattering at the surface/couplant  
153 interface. Such surface machining increases the component processing time and cost, while delaying the inspec-  
154 tion and lowering the throughput. In [29], the components were inspected by a UT probe from below the bottom  
155 base plate [29] and although this method eliminates the need for top surface machining, it is not a viable option  
156 for the increasingly common components which utilize double-sided deposition strategies to minimize residual  
157 stresses and prevent component distortion [36]. Furthermore, a manual ultrasonic inspection of large scale WAAM  
158 components is very time-consuming creating further bottlenecks in production. Additionally, traditional ultraso-  
159 nics probes are typically only functional up to 60 °C, and with the WAAM as-built surface potentially being at  
160 hundreds of degrees Celsius just after the deposition [37] further cooling times and delays are required to be  
161 introduced into the inspection process.

162 The acoustic coupling in ultrasonic inspections is usually established through an acoustic liquid gel, where  
163 a thin layer removes any air gaps between the transducer and the surface due to material roughness or geometrical  
164 unevenness; thus, allowing transmission of the ultrasound wave into the component. Such a liquid gel is however  
165 not ideally suitable for in-situ inspection of WAAM components since it would require a constant supply delivered  
166 to the probe and WAAM surface, likely contaminating the build if a further deposition is required. Despite emerg-  
167 ing water wedges [38] that are capable of conforming to the rough upper surface of WAAM components, still  
168 require an acoustic gel to ensure coupling and allow movement and reduce wear of the probe surface.

169 Non-contact ultrasound inspection techniques such as Laser Induced Phased Arrays (LIPA) [6] and air-cou-  
170 pled UT could bypass these surface coupling challenges, and while LIPA has shown great potential for detecting  
171 small defects in AM components, among its main shortcomings is the need for smooth polished surfaces [39]  
172 inconsistent with the as-built WAAM surface.

173 Contact techniques, that allow transmission of ultrasonic energy into a specimen without the use of liquid  
174 couplants, offer the potential for dry-coupling and reduced surface contamination. Such dry-coupling can be pro-  
175 vided by acoustically matched polymers, which feature low attenuation and wave velocities similar to water [40]  
176 and [41]. When placed between the transducer and the sample and suitable force is applied, the air between the  
177 two mating surfaces is expelled and the acoustic energy is transferred. However, when considering automated  
178 deployment and surface scanning, excessive and damaging shear forces can be introduced from dragging these  
179 polymers across the surface resulting in increased wear and reduced life. A dry-coupled phased array probe, spe-  
180 cifically designed for automated in-process inspection of welds was introduced in [42], which can resist elevated  
181 temperatures and enable rolling motion across surfaces.

182 This body of work presents for the first time an ultrasonic phased array volumetric imaging concept that can  
183 be deployed on the as-built surfaces of WAAM components. Firstly, a dry-coupled contact-based, high-tempera-  
184 ture compliant phased array ultrasound roller-probe for WAAM inspection is introduced. Furthermore, the con-  
185 cept and development behind a three-layer adaptive TFM imaging algorithm is introduced and explained. Finally,  
186 the resultant non-destructive imaging of two titanium WAAM components, with artificial and process defects was  
187 explored and characterized against XCT with a successful correlation between both techniques.

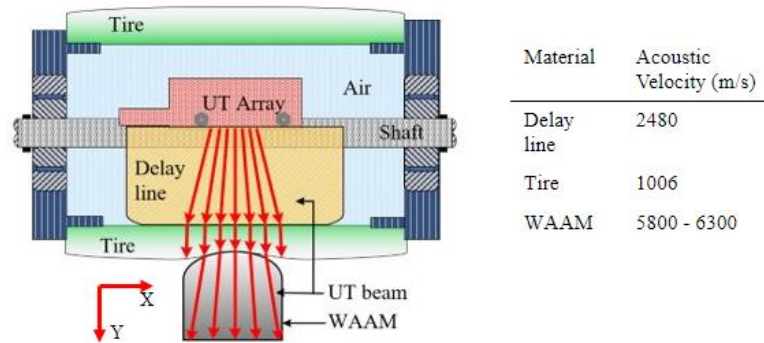
## 188 **2. Dry-Coupled in-situ Ultrasonic Inspection of as-built WAAM Compo-** 189 **nents**

### 190 *2.1: Automated As-Built WAAM Component Inspection*

191 When considering the design and the implementation of an ultrasound probe for in-situ deployment on  
192 as-built WAAM components, two main challenges emerge: (1) Acoustic coupling of the sound into the component  
193 through the as-built surface, and (2) Withstanding the elevated surface temperatures of the as-built component.

194 These challenges can be overcome by using a dry-coupled ultrasonic roller-probe. Conventionally, a  
195 roller-probe is a device with either a single element or a phased array transducer mounted within an acoustically  
196 friendly rubber wheel allowing for faster manual inspection of larger components [41, 43]. Subsequently, the  
197 roller-probe technology has been adapted to the needs for automated inspection of large structures [44, 45]. The  
198 recent development has also shown a deployment of the high-temperature liquid-filled roller-probe on in-process  
199 inspection of multi-pass welds [42]. In this work, a roller-probe is designed for the dry-coupled inspection of large  
200 scale WAAM components in order of centimetres/meters [46] but has the potential to be adapted to a variety of  
201 large scale additive manufacturing techniques or large structures. The WAAM roller-probe, illustrated in Figure  
202 2, is equipped with a watertight rotary rubber tire and a delay-line, through which the ultrasonic wave generated  
203 by the ultrasonic array can propagate. A solid delay line enables conformance of the rubber to the surface of  
204 WAAM by a sufficient amount of force. The ultrasonic array is mounted in the center of the roller-probe on the  
205 delay line. A key advantage of this design can be realized in automated inspection setups, where the rotary design  
206 directly facilitates automated delivery and smooth manipulation over varying profile surfaces at speed. Addition-  
207 ally, the roller-probe is designed to withstand surface temperatures of up to 350°C, meaning it can be deployed  
208 on the WAAM surface just after deposition when the sample is still at elevated temperatures, either in-situ or after  
209 the full built is completed.

210 The WAAM roller-probe is designed to accommodate the mismatch between the flat surface of the delay-  
211 line, inside the roller-probe, and the as-built WAAM surface profile and curvature using the high-temperature  
212 compliant flexible rubber tire. Accordingly, the ultrasound waves generated by the array propagates through three  
213 mediums: 1) the delay line medium, 2) the rubber tire and 3) the WAAM component, as depicted in Figure 2. The  
214 ultrasonic beam refracts at two interfaces namely the delay line/tire and tire/WAAM boundaries with the latter  
215 being a curved interface. Refraction due to any acoustic velocity mismatch between the materials changes the  
216 direction of the beam as it propagates through the layers [47, 48]. Therefore, to compute the precise volumetric  
217 image of the WAAM component, the challenge of ultrasound wave propagation and refraction through three layers  
218 must be addressed.



220

221 **Figure 2** A schematic of the high-temperature roller-probe in contact with a WAAM sample222 *2.2: Automated As-Built WAAM Component Imaging*

223 Ultrasonic imaging and beam tracing through three refractive layers with arbitrary interfaces is difficult to  
 224 overcome using conventional ultrasonic methods such as electronic beamforming [49]. In beamforming imaging,  
 225 the phased array delay laws are calculated prior to the scan to focus the beam at a specific depth through knowledge  
 226 of the material interfaces and then the array is excited using the focal laws to form a B-scan image with fixed  
 227 limited resolution. However, as soon as the curvature of the interface changes during the scan, in this case, the  
 228 WAAM as-built surface, the focal laws require to be recalculated for an optimal beam focus and Signal-to-Noise  
 229 Ratio (SNR). This process requires the continuous online acquisition of the surface profile to constantly update  
 230 the focal laws, greatly affecting scan speed and rendering such methods inefficient for automated applications  
 231 where high scanning speeds are desired. In view of these, alternative fully focused imaging processes that can  
 232 accommodate high scan speeds should be sought for automated inspection applications.

233 Such an objective can be attained through a combination of real-time data acquisition and processing. Full  
 234 Matrix Capture (FMC) is a process where the signal from a full combination of all transmitting and receiving  
 235 combinations are acquired is proposed for future automated inspections. The complete set of time-domain data  
 236 acquired through FMC allows for the implementation of a wide range of post-processing algorithms that seek to  
 237 address all the challenges presented [48].

238 The collected FMC data can then be used to form images using post-processing algorithms, such as the Total  
 239 Focusing Method (TFM), based on Delay-And-Sum (DAS) computational logic, and enabling superior resolution  
 240 and sensitivity to smaller defects when compared to conventional beamforming inspections [50]. The technique  
 241 calculates the Time of Flights (ToF), also called the delays, between each array element and every pixel of the  
 242 image. Based on these delays, the signal amplitudes from the individual A-scans are summed in the final image.  
 243 [50].

244 When considering multiple media inspection, current TFM inspection methods, however, have been mainly  
 245 developed for the two-media inspection of components from either ultrasonic delay-lines placed on the flat sur-  
 246 faces, or wedges on weld plates [51]. When it comes to ultrasonic imaging of components with complex geome-  
 247 tries, the main research focus has been placed on two-media adaptive TFM imaging for immersion (water/sample)  
 248 setups or water-filled conformable delay lines used in contact with complex surfaces [52]. Such two-media algo-  
 249 rithms are application-specific and are not fit for the purpose when considering the three-media inspection of as-  
 250 built WAAM components using the roller-probe introduced above.

251 Therefore, a modified adaptive TFM algorithm is proposed herein to account for the three mediums (delay-  
 252 line, tire and WAAM component) and the two interfaces with compensation for the as-built WAAM surface cur-  
 253 vature. The performance of the algorithm is then assessed through imaging and inspection of as-built Ti-64  
 254 WAAM components with both Bottom-drilled Holes (BH) and intentional LoF defects. The LoF defects were  
 255 also scanned using micro-focus XCT to verify and compare the results of the adaptive TFM algorithm.

256 *2.3: Ultrasonic Imaging through Arbitrary Unknown Surfaces*

257 To be able to form TFM images of the WAAM components after FMC acquisition, the geometry of the  
 258 unknown interfaces should be identified. Given the known and flat delay-line/tire interface, it is only necessary to

259 include a stage to reconstruct the tire/WAAM interface surface profile. The surface finding algorithm developed  
 260 for this work is based on a dual-medium Synthetic Aperture Focusing Technique (SAFT) imaging.

261 Utilizing SAFT instead of TFM for the surface imaging was studied in [53], where TFM was not able to  
 262 present a full contour of the tested specimen due to the high-intensity side lobes, while SAFT presented a clean  
 263 contour without disruption by false signals.

264 Like TFM, the SAFT imaging is a DAS post-processing algorithm that employs a sub-aperture of elements  
 265 for constructing an image. In the SAFT algorithm, the contribution of elements to the image pixels is predeter-  
 266 mined by the angle intervals. Once the image is computed, a surface profile is extracted autonomously by isolating  
 267 the pixels with the signal intensity above a threshold and fitting a curve. Achieving a high precision surface profile  
 268 is an important step in this work as even minor profile errors could result in loss of image quality due to loss of  
 269 focus coherence in the final TFM imaging stage [54].

270 In this paper, for the first time, a novel hybrid SAFT and TFM algorithm was developed to identify the  
 271 unknown as-built WAAM surface and compute a TFM image of the cross-sectional WAAM wall while inspecting  
 272 through 3-layers. Contact ultrasound inspection and FMC data collection were made possible owing to the inno-  
 273 vative high-temperature phased array roller-probe design that is conformable to the as-built surface of the WAAM  
 274 components. The hybrid SAFT + TFM algorithm together with the roller-probe were combined to form a unified  
 275 inspection methodology for automated high-speed inspection and imaging of WAAM components.

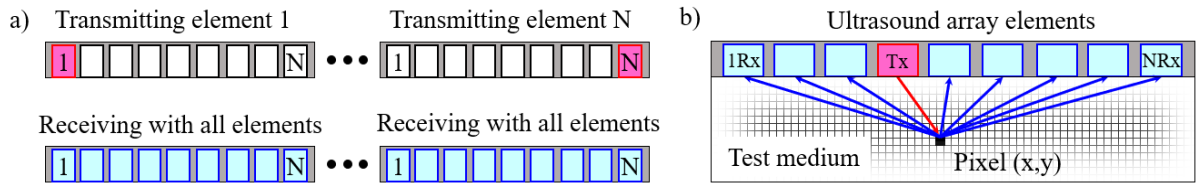
276

### 277 3. Ultrasonic Imaging through Three-layers and Arbitrary Complex Sur- 278 faces

#### 279 3.1 The Full Matrix Capture (FMC) and Total Focusing Method (TFM)

280 Ultrasonic arrays were used for the data acquisition process, where time-domain signals from every pair  
 281 of the transmit (Tx) -receive (Rx) elements were collected to form the FMC dataset. For a linear array with  $N$   
 282 elements, a total number  $N^2$  A-scans were recorded. The illustrations of Figure 3(a) show the sequence of trans-  
 283 mit-receive elements activated in an FMC acquisition mode where a single transmit element was stepped by 1  
 284 between 1 to  $N$ , and for each transmission, all the  $N$  elements were used in the reception.

285



287

**Figure 3** Diagram explaining (a) full matrix capture data collection, and (b) total focusing method

288 The FMC dataset served as the input to the TFM images that were subsequently processed using a DAS  
 289 algorithm. In the TFM algorithm presented here, the full aperture of the array was used to synthesize a focus on  
 290 every pixel of the image at both the transmission and the reception stages, as shown in Figure 3(b), allowing  
 291 higher resolution across the whole image, and therefore, a higher sensitivity to smaller defects. For every image  
 292 pixel  $P$  within the inspection medium, the image pixel intensity  $I(P)$  for each transmit-receive  $(k, l)$  combination  
 293 was calculated through:

$$I(P) = \sum_{k=1}^N \sum_{l=1}^N S_{k,l} (T_{Tx(k)} + T_{Rx(l)}) \quad (1)$$

294 where,  $S_{k,l}$  is the time-trace associated with the A-scan of every Tx-Rx combination,  $T_{Tx(k)}$  represents a  
 295 ToF from the transmitted element to the pixel P, and  $T_{Rx(l)}$  stands for the return journey from the pixel P to the  
 296 element. A TFM image frame  $(I_{(i,j)})$ , with grid point indexes  $(i, j)$ , was computed using the elementary A-scans  
 297 within the FMC dataset, while a secondary one  $(I'_{(i,j)})$  was also obtained through a Hilbert transform of the A-

300 scans with the application of the same delays. Consequently, the TFM envelope ( $I_{envelope}$ ) was calculated using  
 301 the following formula:

$$|I_{envelope}| = \sqrt{(I_{(i,j)})^2 + (I'_{(i,j)})^2} \quad (2)$$

302 Therefore, the resulting image was composed of two TFM images: (I) one produced from the real component  
 303 of the elementary A-scans, and (II) the other from the imaginary component of the elementary A-scans. The main  
 304 advantage of the enveloped image lies in the possibility of increasing the grid pixel size, and hence, curtailing the  
 305 computation time needed to compute the image without losing the intensity of the signal [55]. Finally, to present  
 the pixels in a dB scale with the reference to the maximum amplitude of the image, the pixel amplitude  $I_{amp}$   
 values were normalized by the maximum amplitude  $I_{amp\_max}$  present in the image as shown in Equation 3.

$$I_{amp\_norm} = 20 \times \log_{10}\left(\frac{I_{amp}}{I_{amp\_max}}\right) \quad (3)$$

306

### 307 3.2. Focusing Through Multiple Media

308 This body of work aims to implement TFM imaging of WAAM components through three mediums and  
 309 across two interfaces. These are the fixed planar delay-line/tire interface inside the PAUT probe and the non-  
 310 planar tire/WAAM arbitrary contour interface on the as-built WAAM surface. The delay calculations were carried  
 311 out according to the minimum ToF principle, which is also known as Fermat's principle [56]. In the case of  
 312 homogeneous media, a straight line connecting an element and an image pixel best describes the path along which  
 313 an ultrasonic wave generated by the element traverses to reach a specific image pixel. However, when a media  
 314 constituted of multi-materials with different acoustic properties is considered, the ultrasonic waves generated by  
 315 the elements refract across the interfaces before reaching the image pixel in the target medium; hence, the orien-  
 316 tation of the wave travelling path varies in each medium. To this end, the ToF's should be calculated individually  
 317 in each medium as illustrated in Figure 4. In the cartesian coordinates, the algorithm for ToF  $T_{(Tx,Rx)}$  for both Tx  
 318 and Rx array elements to pixel P ( $x, y$ ) in the WAAM component can be formulated as:

$$T_{(Tx,Rx)} = \frac{\sqrt{(x_{i1} - x_t)^2 + (y_{i1} - y_t)^2}}{v_1} + \frac{\sqrt{(x_{i2} - x_{i1})^2 + (y_{i2} - y_{i1})^2}}{v_2} + \frac{\sqrt{(x_p - x_{i2})^2 + (y_p - y_{i2})^2}}{v_3} \quad (4)$$

319

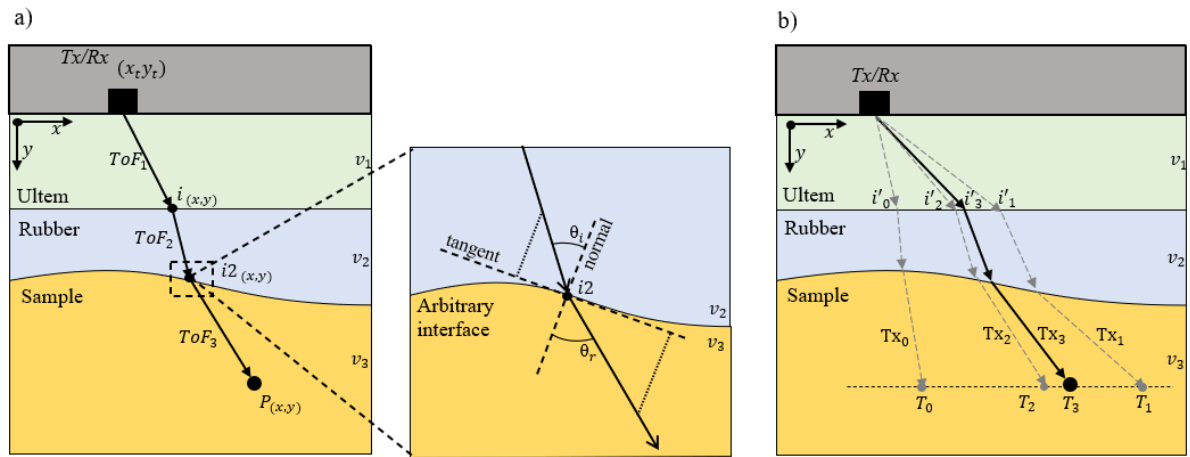
320 where the  $(x_t, y_t)$ , the  $(x_{i1}, y_{i1})$ , the  $(x_{i2}, y_{i2})$ , and  $(x_p, y_p)$  are respectively, the coordinates of the  
 321 array elements, the incidence point of the ultrasound ray to the first interface, the incidence point of the ultrasound  
 322 ray to the second interface, and the targeted pixel. The  $(v_1)$ ,  $(v_2)$  and  $(v_3)$  are the velocities in the first, second  
 323 and third medium.

324 The wave refraction angles at the interfaces were also calculated using Snell's law which is presented in  
 325 its most common form in Equation 5, where  $\theta_i$  and  $\theta_r$  represent the angles of the incidence and the refraction,  
 326 respectively, as illustrated in Figure 4(a). It should be noted that the refraction angle at the incidence point on the  
 327 arbitrary profile was also calculated with respect to the normal of the surface at the point illustrated in Figure 4.  
 328

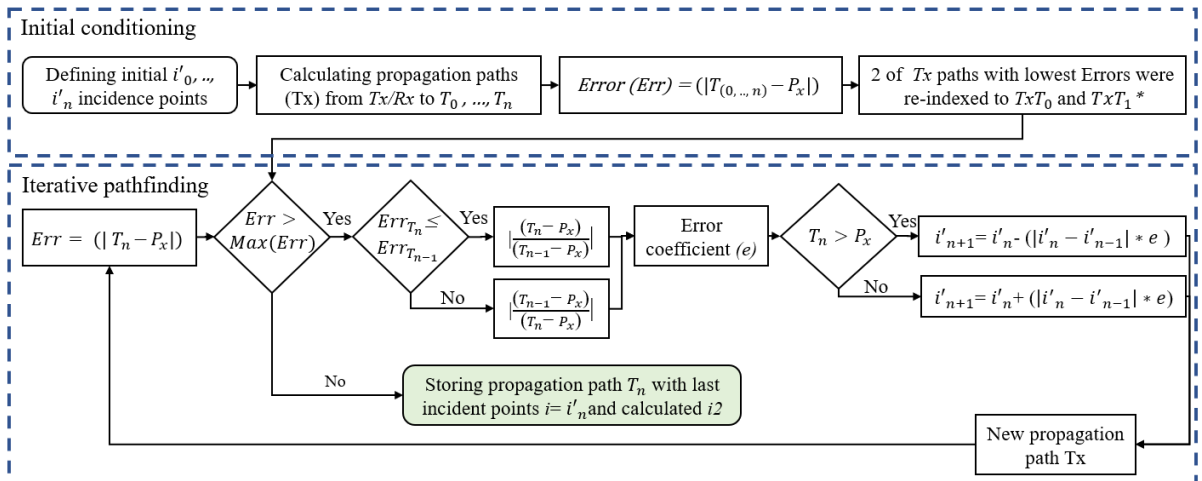
$$\frac{\sin(\theta_i)}{v_1} = \frac{\sin(\theta_r)}{v_2} \quad (5)$$

329 In this work, a root-finding algorithm based on a bisection method was developed and used to trace the  
 330 ultrasound ray path between the array elements and the image pixels to a precision defined by the user. Clearly,  
 331 higher precision demands a longer algorithm runtime due to the increased number of iterations required to con-  
 332 verge to a solution. The ray-tracing workflow used within the algorithm is shown in Figure 5(b) and demonstrated  
 333 in Figure 4(b), and can be summarized in the following steps:

- 334 1. At the first interface (delay-line/tire), evenly distanced finite number of nodes ( $i'_n$ ) are initially generated.
- 335 2. The ray ( $Tx_n$ ), with ( $n=Node\ number\ on\ the\ first\ interface$ ), transmitted from an element is connected to
- 336 each of the nodes with the straight lines and the refracted angles calculated at the first interface and at each
- 337 node.
- 338 3. The point coordinates at which the rays refracted from the first interface impinge the second interface are
- 339 found, and the resulting refraction angles from the second interface are obtained.
- 340 4. The  $T_0, \dots, T_n$  points where the rays refracted from the second interface ( $i_2$ ) approach the pixel's  $y$  coordinate
- 341 are indicated and the positional error of the rays in the  $x$ -direction with the reference to the target pixel
- 342 assessed. Subsequently, the two coordinates closest to the pixel of the pixel are selected while the rest of
- 343 them are discarded.
- 344 5. If the error is larger than the maximum allowed distance between an incoming ray and the pixel point, a new
- 345  $i'$  is selected. Otherwise, the path with the lower error is stored and a new pixel-element pair calculated.
- 346 6. To select a new  $i'_n$ , the error coefficient ( $c$ ) is obtained as an absolute value of the division of the two errors
- 347 between  $T_0, T_1$  and targeted pixel. It is necessary to make sure that  $0 \leq c \leq 1$ , thus a larger error is always
- 348 divided by a smaller value.
- 349 7. The coefficients are then applied, where the distance between two previously used  $i'_n$  and  $i'_{n-1}$  are sub-
- 350 tracted and multiplied by the coefficient, giving a new offset. Subsequently, this offset is added or subtracted
- 351 from the latest  $i'_n$  depending on whether the  $T_n$  is larger or smaller than a targeted pixel.
- 352 8. The process is iterated until the distance measured between the  $T_n$  and the pixel becomes smaller than the
- 353 error indicated. This yields the ray path ( $Tx$ ) and the ToF from an element to a pixel in the image.
- 354 9. The process is repeated until the ToF's for all the combinations of elements and pixels is reached.



355 **Figure 4** Schematic diagram showing a) ray tracing and time of flight calculations between an array element  
 356 and a target pixel through three media with refractions on planar (delay-line/tire) and non-planar (tire/WAAM)  
 357 interfaces, and b) iterative process and convergence to a target pixel using the search algorithm.  
 358



359 **Figure 5** Diagram explaining the search algorithm developed for ultrasonic ray-tracing  
 360

### 3.3.1 Ultrasonic Driven WAAM Surface Reconstruction

361

362

363

364

365

366

367

368

369

The first step taken in the imaging process is to estimate the surface profile of the WAAM component. Knowing the planar interface (delay line/tire), the WAAM interface region can then be imaged directly. For this purpose, a dual-medium (*i.e.* propagation through the delay-line towards the bottom of the tire) DAS SAFT algorithm with angular aperture limit was developed. The limitation is defined by  $\alpha$  and  $\beta$  marking the angles between the outmost rays focused at each pixel and the normal of the first interface, as depicted in Figure 6. The intensity of each pixel  $P$  in the image was computed using the velocity of the first ( $v_1$ ) and second ( $v_2$ ) media only, and given by:

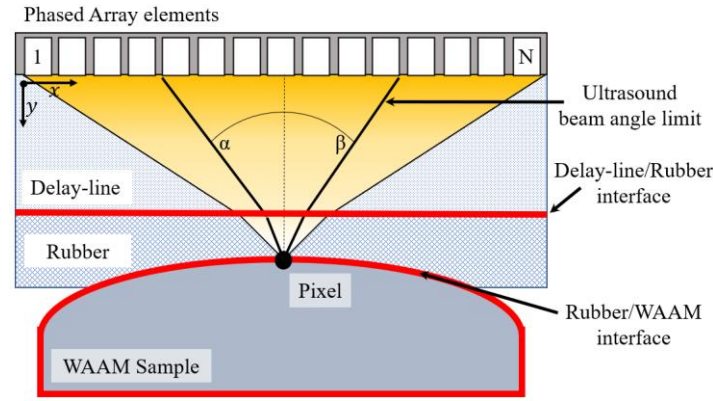
$$I_{rubber}(P) = \sum_{k=1}^N \sum_{l=\alpha}^{\beta} S_{k,l} (T_{Tx(k)} + T_{Rx(l)}) \quad (6)$$

370

Where,  $T_{(Tx,Rx)}$  was calculated in coordinate system  $(x, y)$  and was given by:

$$T_{(Tx,Rx)} = \frac{\sqrt{(x_1 - x_t)^2 + (y_{i1} - y_t)^2}}{v_1} + \frac{\sqrt{(x_{i2} - x_{i1})^2 + (y_{i2} - y_{i1})^2}}{v_2} \quad (7)$$

371



372

373

374

375

376

**Figure 6** Diagram illustrating the phased array elements contribution to the pixel of the SAFT image targeting the tire/WAAM interface, and limited by the angles  $\alpha$  and  $\beta$

### 3.3.2 Ultrasonic Driven WAAM Surface Profile Extraction

377

378

379

380

381

382

383

384

385

386

Once the surface image is generated, global thresholding is used to extract the surface points. The algorithm is designed for automated surface reconstruction sweeps of the image, column by column, to identify the pixels with the highest intensity value above the defined threshold. If two identical values coexist in the same column, the algorithm retains the pixel with the lower  $y$  coordinate in Figure 10 (c). This is introduced to prevent the occurrence of errors due to stronger signals received from the inside of the specimen or attributed to the second reflection. Knowing the characteristic surface finish of WAAM builds deposited with common deposition strategies, which typically represent a semi-elliptical shape with waviness, the extracted pixels were sufficiently defined with a 4<sup>th</sup> order polynomial curve, smoothed by the local polynomial regression also known as moving regression. Smoothing of the curve was necessary to avoid potential distortions of the curve caused by dislocated surface points wherever a false echo is present in the surface image.

387

## 4 Experimental Setup

388

### 4.1 Phased Array Ultrasonic Inspection Configuration

389

390

The ultrasonic roller-probe used in the experiments encompassed a 5 MHz 64 element linear array with specifications presented in Table 1.

391

**Table 1** phased array probe parameters

Array Parameters	Value
Element Count	64
Element Pitch	0.5 mm
Element Elevation	10 mm
Element Spacing	0.1 mm
Centre Frequency	5 MHz

392

393

394

395

396

397

398

399

400

401

402

The array transducer was mounted on a 26 mm high delay-line with a density of  $1.27 \text{ g/cm}^3$  and an acoustic velocity of  $2480 \text{ ms}^{-1}$  inside the roller-probe. A liquid gel was used as the couplant at the interfaces of the array/delay-line and the delay-line/tire. A 6 mm thick, soft silicone rubber tire, with high-temperature compliance ( $350 \text{ }^\circ\text{C}$ ) constituted the exterior layer of the roller-probe [57]. Figure 7 demonstrates the experimental setup where the roller-probe was mounted on a 7-axis KUKA LBR robotic arm that featured embedded force-torque sensors in its joints. The robot provides the force-torque values of the end effector, and this feature was used to ensure a constant contact force of 50 N between the roller-probe and the WAAM component. FMC data was collected at 12-bit resolution using a Peak NDT LTPA phased array controller with 200 V excitation voltage and fixed hardware gain of 65 dB. The time-domain matrix of the signals was formed by 8000 data samples for each transmit-receive pair A-scan at a sampling frequency of 50 MHz.

403

404

405

406

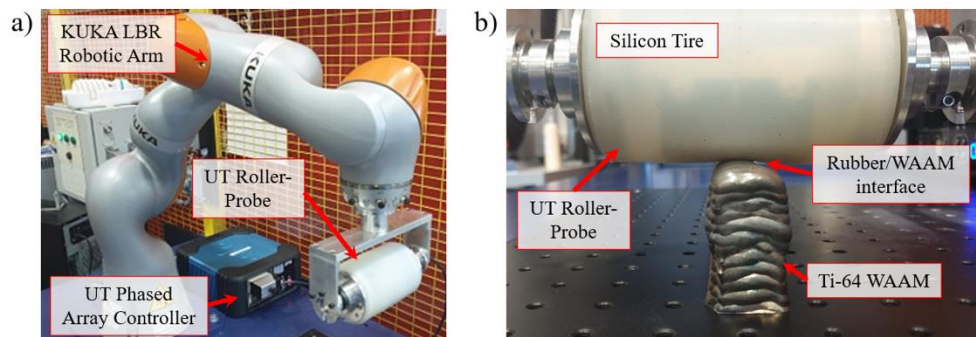
407

408

409

410

The SAFT surface identification and TFM imaging algorithms were integrated and implemented in MATLAB 2020a. The processing time was evaluated on an AMD Ryzen Threadripper 3960 24 core Processor with a clock speed of 3.79 GHz and 128 Gb of Random-Access Memory. The elapsed time for the SAFT algorithm to estimate the surface contour was 3.1 seconds, and the convergence for the ray tracing and the TFM image creation was 30 seconds. Although in this work the speed of the algorithm was not the prime importance and was not optimized, further modifications will be investigated to leverage the computing power of Graphics Processing Units (GPU) and to minimize this computation time. Optimizing for GPU usage can offer the advantage of splitting the execution on a much higher number of cores compared to a low number of CPU cores.



411

412

413

**Figure 7** Robotic ultrasonic inspection set-up consisting of (a) a KUKA robotic arm, ultrasound phased array controller, and (b) an ultrasonic roller-probe placed on a titanium WAAM sample

414

#### 4.2 Process Flow of In-Situ Imaging of As-Built WAAM Components

415

416

417

418

419

420

Figure 8 shows the imaging process flow where the images for a surface finding algorithm were built to have 10 pixels per image millimeter of the image generating a grid of  $320 \times 60$  pixels. The height of the imaging window was selected as 5 mm, to enclose the entire span of the tire/WAAM interface, where the surface profile was expected to lie. The final adaptive TFM images were computed using 5 pixels per image millimeter, thus the verification sample was imaged using a grid of  $160 \times 75$  pixels and the defective titanium wall imaged using  $100 \times 50$  pixels, optimized from coarser larger areas scans.

421

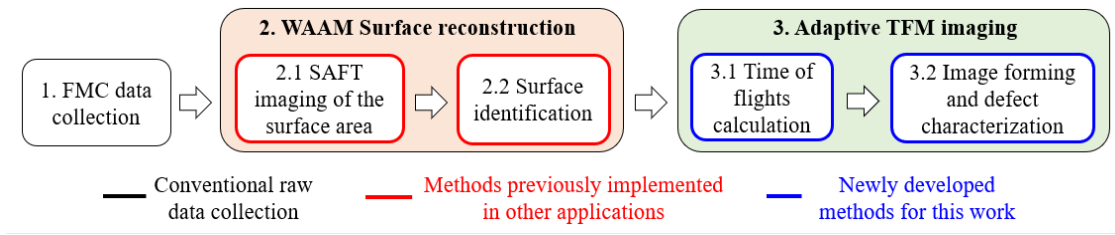
422

423

424

The SAFT surface images were processed assuming constant longitudinal wave velocities of  $2480 \text{ ms}^{-1}$  for the delay-line and  $1006 \text{ ms}^{-1}$  for the rubber, both measured experimentally. Once the tire/WAAM interface was identified via the SAFT algorithm, the ToF's through the three mediums were computed to construct the adaptive TFM images with the additional longitudinal velocity of the titanium ( $6100 \text{ ms}^{-1}$ ). The velocity values

425 were found without significant variations after the measurements in pulse-echo mode using single element trans-  
 426 ducers.



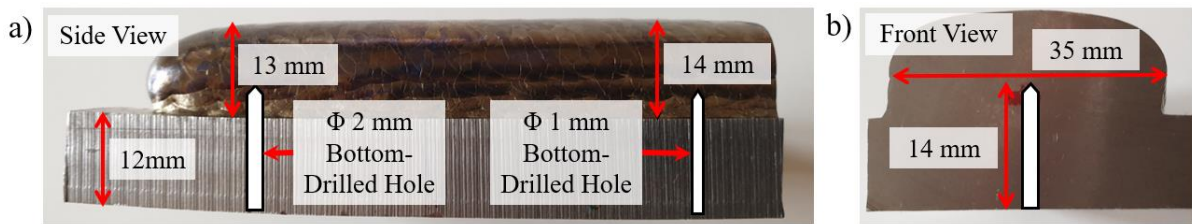
427

428 **Figure 8** Diagram illustrating the SAFT surface finding and TFM imaging processing of the collected FMC data

## 429 **5 Automated Dry-Coupled In-Situ Ultrasonic Inspection of As-Built Tita-** 430 **ni-um WAAM Components**

### 431 *5.1 Titanium WAAM Verification Wall with Artificially Drilled Reflectors*

432 An initial experiment was conducted on a Ti-64 test specimen manufactured using the plasma arc  
 433 WAAM process and oscillation deposition strategy. Five layers with an approximate height of 2.5 mm per layer  
 434 and a width of 35 mm were deposited on a 12 mm thick base plate. Two artificial defects were fabricated in the  
 435 form of Bottom-drilled Holes (BH) with diameters of 1 mm and 2 mm respectively and extending up by 14 mm  
 436 into the sample, as shown in Figure 9.



437

438 **Figure 9** (a) Side view and (b) front view of a WAAM Ti-64 component deposited using oscillation strategy  
 439 and containing fabricated calibration bottom-drilled holes of 1 mm and 2 mm in diameter

### 440 *5.1.2 Titanium WAAM Verification Wall Surface Reconstruction*

441 The FMC dataset corresponding to the sample with 2 mm BH was processed and analyzed for the  
 442 WAAM surface profile estimation. For the SAFT processes used in this paper, the images were calculated using  
 443 an angle limitation  $\alpha = -7.5^\circ$  and  $\beta = 7.5^\circ$  which was found to be the most accurate during initial trials and the image  
 444 dB scale set to 0 to -30 to best visualize individual features of the image without noise disturbance.

445 A clear representation of the contour of the WAAM surface (dashed green box) can be observed on the  
 446 SAFT image in Figure 10 (a). Furthermore, a strong signal indicating the end of the coupling area between the  
 447 roller-probe's tire and the WAAM surface (*i.e.*, decoupling points) are also visible and marked (dashed red box).  
 448 Below the surface contour in the image, the repeated signal of the tire/sample interface can also be seen (dashed  
 449 yellow box).

450 Prior to deploying the WAAM surface finding, it was necessary to separate the signal of the WAAM  
 451 contour from the signal received for decoupling points. The coupled width of the tire/WAAM interface was found  
 452 to be 30 mm, obtained from measuring the distance between the decoupling points and used to determine the  
 453 maximum width over which the curve fitting was performed.

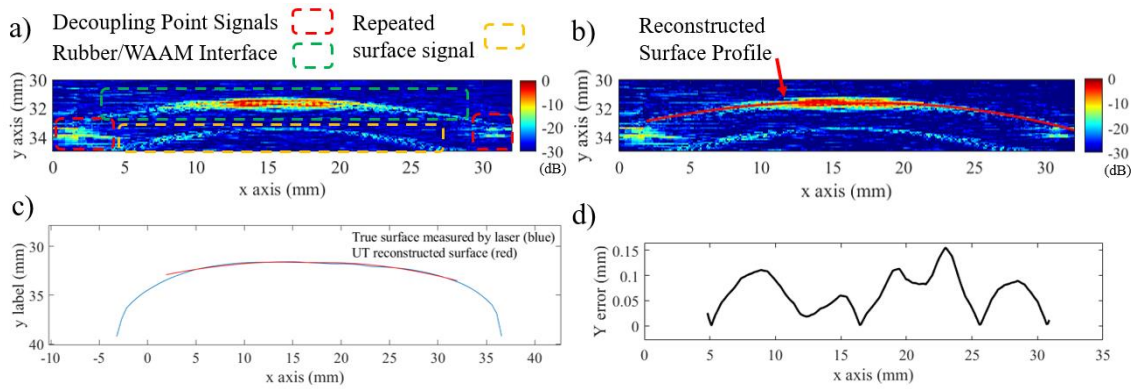
454 Signal amplitudes lower than -10 dB of the maximum image amplitude were then filtered to discard any  
 455 noise from the image. Owing to the thresholding, the image pixels with the highest signal amplitudes were suc-  
 456 cessfully identified and a curve fitted through them to represent the WAAM surface, as shown in Figure 10 (b).  
 457 The SAFT surface finding performance was evaluated by comparing the reconstructed surface against surface  
 458 profiles obtained via a non-contact metrology laser scan with a y-axis resolution of 12  $\mu\text{m}$  [58] (Figure 10 (c)).  
 459 The total number of points along the x-axis for the profile acquired by the laser was 300 resulting in a spatial

460 sampling of 0.1 mm. To quantify the discrepancy between the two curves, the average error between the two  
 461 profiles was calculated through:

$$\Delta_{average} = \frac{1}{k} \sum_{k=1}^{k=n} |Y_{True}^k - Y_{UT}^k| \quad (8)$$

462 where  $n$  is the total number of points used in the curve fitting ( $n = 300$ ),  $k$  is the point number along the  
 463  $x$ -axis of both the true surface profile and the SAFT estimated surface profile, and  $Y$  stands for the  $y$ -axis position  
 464 of points. The calculation was only performed within an interval where both surfaces exist. The average error  
 465 between the profiles (visualized in Figure 10 (d)) was calculated using Equation 8 as 0.06 mm. It is worth noting,  
 466 that given the phased array sampling frequency of 50 MHz and the longitudinal wave velocity of Ti-64 (velocity  
 467 =  $6100 \text{ ms}^{-1}$ ) results in a distance resolution of a minimum 0.12 mm within the Ti-64 medium; double the devel-  
 468 oped SAFT surface reconstruction algorithm resolution.

469



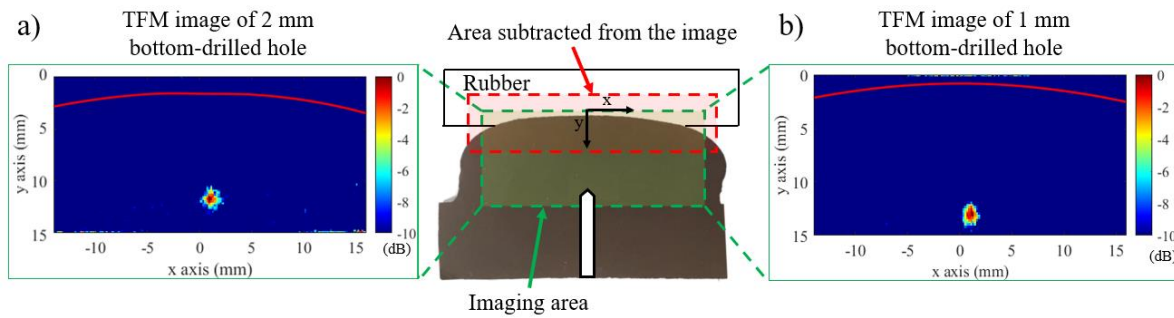
470

471 **Figure 10** (a) An image of the WAAM surface formed using the dual-medium SAFT algorithm, (b) fitted curve  
 472 to the extracted high-intensity surface points of the SAFT image after filtering and denoising, (c) comparison  
 473 between the laser-scanned surface profile and the SAFT reconstructed profile, and (d) measured error between  
 474 the surface profile acquired by laser and through SAFT reconstruction of the Ti-64 WAAM with bottom-drilled  
 475 holes

### 476 5.1.3 Titanium WAAM Verification Wall TFM Image Reconstruction

477 Figure 11 depicts the results of the TFM imaging for the two BHs in the Ti-64 WAAM sample, after  
 478 incorporating the reconstructed WAAM surface profile estimated in Section 5.1.2. This figure displays the two  
 479 imaged sections of the WAAM component located immediately beneath the roller-probe and the two BHs. The  
 480 TFM images reconstructed from this data are shown in the green box in Figures 11 (a) and (b) for BHs of 2 mm  
 481 and 1 mm, respectively. As demonstrated in the figure, both the 1 mm and 2 mm defects were successfully detected  
 482 and their indications evident in the reconstructed TFM images. To facilitate the detectability, the area in the im-  
 483 mediate vicinity of the defect was windowed to exclude the surface signal and its trailing noise from the compu-  
 484 tation.

485 In order to size the defects, a horizontal line parallel to the  $x$ -axis and passing through the pixel with the  
 486 highest defect signal was selected in each of the TFM images, and the pixel values along this line were plotted in  
 487 Figure 12. The analysis was carried out using the 6-dB drop technique, recognized as a conventional flaw sizing  
 488 methodology in ultrasound inspections [59]. This was achieved by superimposing a horizontal line through the  
 489 intensity plots at a level where the amplitude reduces by 6dB from the maximum signal amplitude of the defect  
 490 and measuring the distance between the intersection points. The lengths measured were 1.3mm and 1.88 mm for  
 491 1mm and 2mm defect, respectively.



492

493

494

**Figure 11** TFM image reconstructions for bottom-drilled holes of: (a) 2 mm, and (b) 1 mm in diameter inside a Ti-64 WAAM component

495

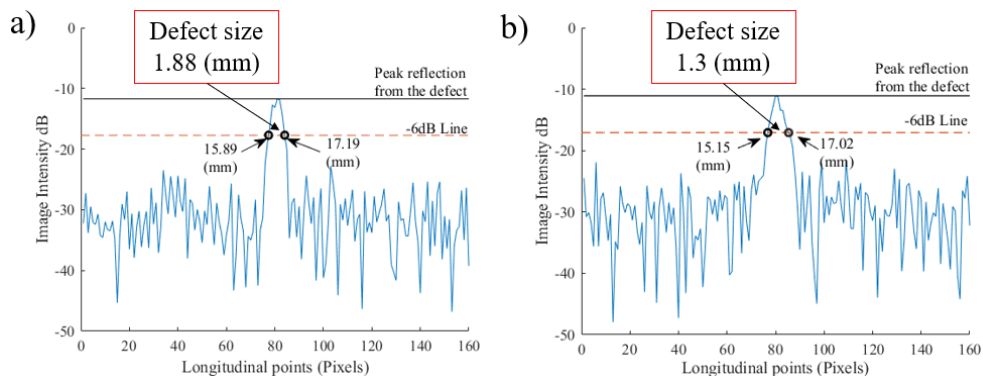
496

497

498

499

For the images of Figure 12, SNR was calculated to assess the overall image quality and detection capability of the inspection configuration. To this end, the root mean square of the noise data presented in the plots of Figure 12, excluding the signal of the defect, was calculated to indicate the noise level. Subsequently, the SNR was obtained as the ratio of the maximum defect amplitude to the average noise level. It can be observed from the results of Figures 11 and 12 that an SNR of at least 15 dB was achieved for the smallest defect.



500

501

502

503

**Figure 12** Pixel intensity values plotted alongside horizontal lines at -6 dB of the maximum image amplitudes passing through the maximum signals of a) 2 mm and b) 1 mm defects to size defects indications

504

### 5.2.1 Titanium WAAM with Artificially Induced LoF Defects

505

506

507

508

509

510

511

512

513

514

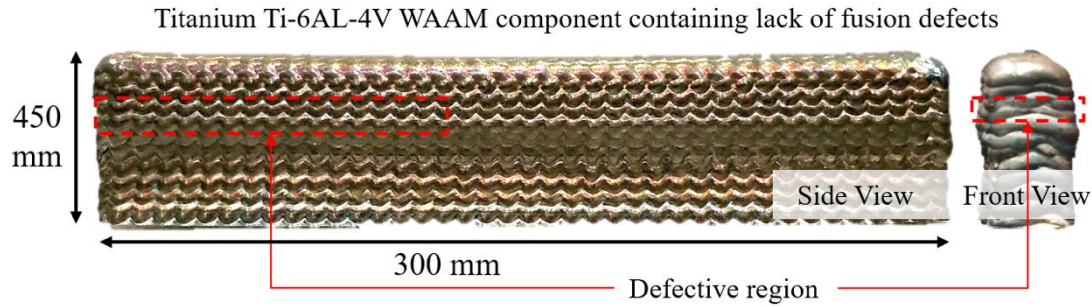
515

516

517

518

After successful verification on the above sample with artificial defects, experiments were also carried out on a Ti-64 WAAM wall (Figure 13), deposited with an oscillation strategy containing intentionally induced defects. The component (45 x 25 x 300 mm (H x W x L)) had intentional LoF defects introduced during the process at layer 6, located 30 mm above the baseplate, by decreasing the arc current from 100% to 70% and increasing the travel speed from 100% to 125%. For the next layer, the welding current was restored to 100% again, but the travel and the wire feeding speeds were reduced from 100% to 70% to repair the morphology of the previous layer. This process was used to smoothen the discontinuities generated within the previous layer and to maintain the final shape of the component, however, despite the repair process, some LoF defects were expected to remain in the component. To verify the existence of these defects, reference XCT tests were conducted using a Nikon XT H 225/320 LC X-ray computer tomography system fitted with a 225kV X-ray source. A maximum resolution of 100  $\mu\text{m}$  was achieved, given the dimensions of the Ti-64 component, its placement within the XCT chamber, and its distance from the X-ray source. The wall was then inspected using the PAUT roller-probe and FMC data collected to compare with the XCT data.



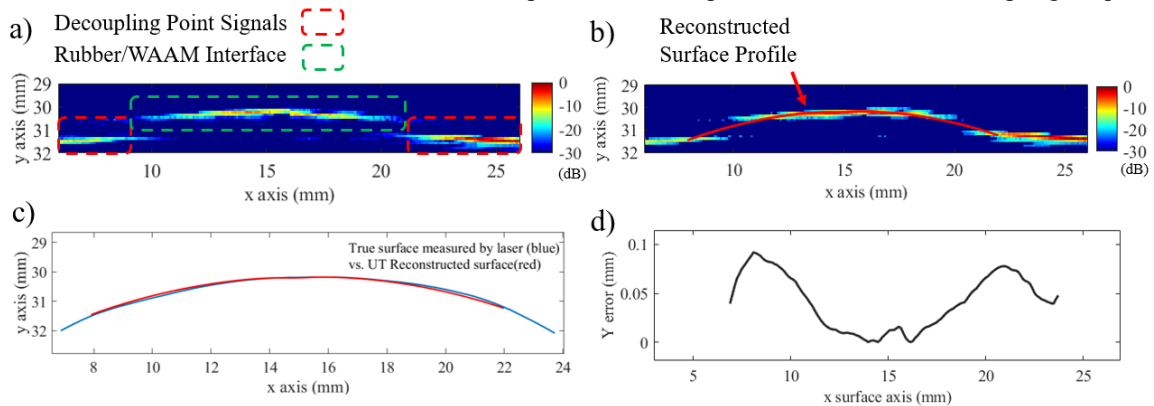
519

520 **Figure 13** Ti-64 WAAM specimen deposited by oscillation strategy and containing process-induced intentional  
 521 deposition lack of fusion defects spread over the marked area

### 522 5.2.2 Titanium WAAM with Artificially Induced LoF Defects Surface Reconstruction

523 The FMC dataset acquired was also analyzed using the SAFT algorithm to estimate the surface contour  
 524 and the results presented in Figure 14. A strong indication of the WAAM surface, as well as reflections of the  
 525 decoupling points, were clearly distinguishable (Figure 14 (a)). Following the same procedure described in Sec-  
 526 tion 5.1.2 for the SAFT images, the width of the contact area was determined (15 mm), the image filtered for  
 527 amplitudes lower than -10 dB of the maximum and a 4<sup>th</sup> order polynomial fitted to the high-intensity surface points  
 528 as depicted in Figure 14 (b).

529 Again, the SAFT surface finding performance was evaluated by comparing the reconstructed surface  
 530 against surface profiles obtained via a non-contact metrology laser scan [58] and the average surface estimation  
 531 error, presented in Figure 14 (d), was calculated to be 0.04 mm. Moreover, it can be seen in Figure 14 (d) that a  
 532 lower surface mismatch was observed at the center of the two profiles where the tire was fully coupled to the peak  
 533 of the WAAM surface. This may suggest better performance of the algorithm for the surface points closer to the  
 534 center of the array. Although the error value continued to grow towards the corners of the WAAM, reaching up  
 535 to 0.09 mm, it was still smaller than the ultrasonic spatial resolution permissible at the fixed sampling frequency.



536

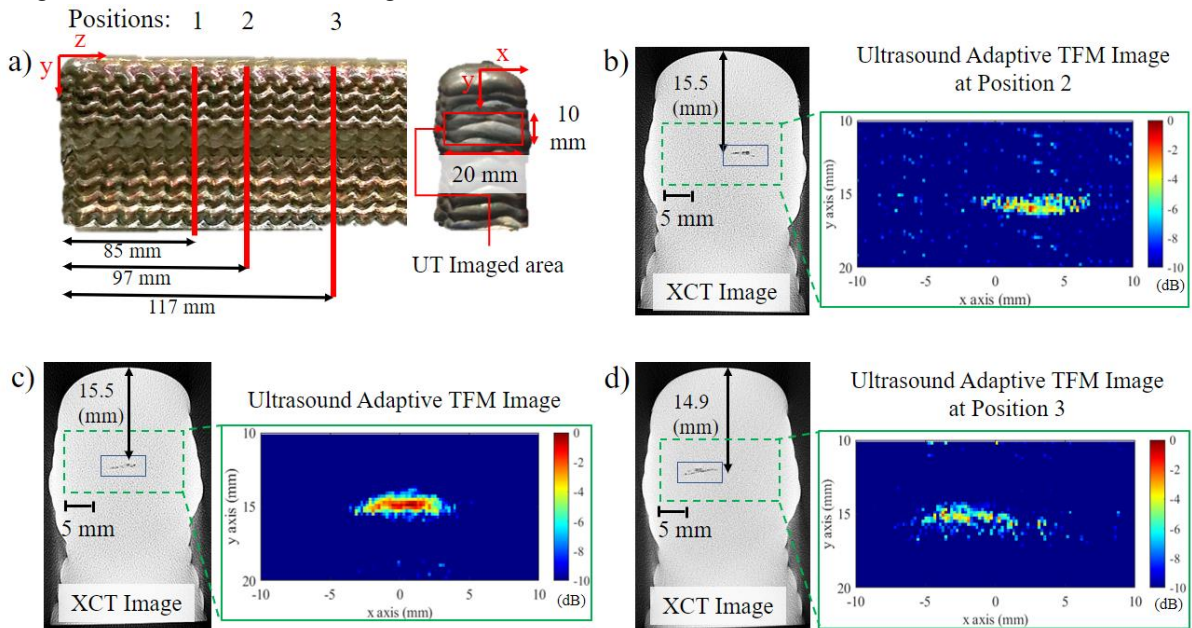
537 **Figure 14** (a) An image of the WAAM surface formed using the dual-medium SAFT algorithm, (b) fitted curve  
 538 to the extracted high-intensity surface points of the SAFT image after filtering and denoising, (c) comparison  
 539 between the laser-scanned surface profile and the SAFT reconstructed profile, and (d) measured error between  
 540 the surface profile acquired by laser and through SAFT reconstruction of the Ti-64 WAAM with intentional de-  
 541 fects

### 542 5.2.3 Titanium WAAM with Artificially Induced LoF Defects TFM Image Reconstruction

543 Figure 15 (a) shows three inspection positions, correspondingly aligned to the areas with induced pro-  
 544 cess-driven defects and which possessed the highest signal amplitude in the acquired ultrasonic data stream. The  
 545 surface profiles were calculated at these points and the TFM images were computed for a rectangular area of 10  
 546 mm by 20 mm across the  $y$  and  $x$ -axes, respectively. The images were normalized by the maximum signal ampli-  
 547 tude and plotted on a 10 dB scale in Figure 15.

548 Figures 15 (b), (c), and (d) show that the ultrasonic indications of the three LoF defects, located at dif-  
 549 ferent positions in the Ti-64 WAAM were readily detectable in the resultant TFM images. For the reference XCT  
 550 images, a full 3D model of the WAAM component was reconstructed, the model sliced at the corresponding TFM

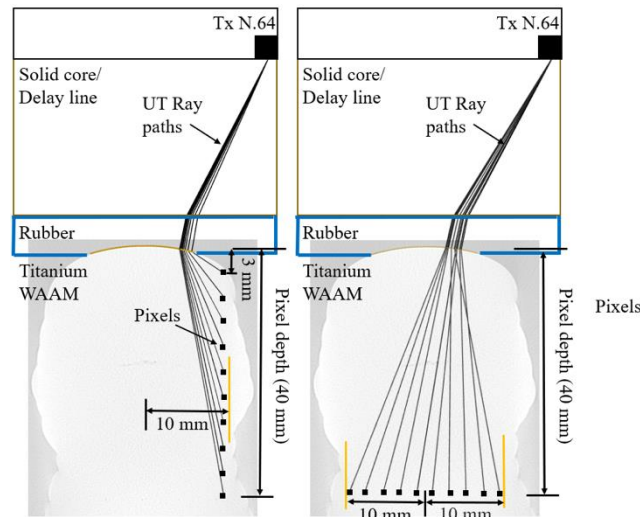
551 image location along the z-axis, and a 2D grayscale representation of the defect was processed. The TFM results  
 552 were then compared with those obtained from the XCT analysis in the same location. To aid readability, the TFM  
 553 images corresponding to each of the defects on the XCT frames are presented in a green rectangular window  
 554 beside their XCT counterpart. The dimensions of the targeted defects were measured from the XCT images to be  
 555 approximately 0.5 x 6 x 0.5 mm (H x W x L). It is The SNR of the images was measured to be a minimum of 10  
 556 dB which is deemed acceptable, given the coupling method, surface waviness and attenuation within the roller-  
 557 probe's tire. Moreover, it is worth mentioning that the defects themselves are not pure cavities but fragmented,  
 558 varying in shape and thus, signal retrieved must therefore be considered adequate. In terms of defect locations,  
 559 good agreement was found between the depth and the horizontal position of the defects measured from the TFM  
 560 images and those from the XCT images.



561  
 562 **Figure 15** (a) Roller-probe Ti-64 WAAM inspection positions where FMC data sets were collected, and a compar-  
 563 ison between the results of adaptive TFM imaging and those obtained by XCT tests for the defects at posi-  
 564 tions (b) 1, (c) 2, and (d) 3

#### 565 5.2.4 Automated As-Built WAAM Component Ultrasonic Volumetric Coverage Considerations

566 One further advantage of the DAS TFM algorithm proposed in this study can be summarised by referring  
 567 to the raytracing diagram presented for the last element of the array in Figure 16. As the Figure suggests, even the  
 568 waves generated by the array elements located at the extremities of the active aperture have significant contribu-  
 569 tions to the final TFM image. This is particularly interesting when tracing the ray from element 64 to the lateral  
 570 pixels (Figure 16(a)) and bottom pixels located 40 mm inside the sample (Figure 16 (b)), showing that the refrac-  
 571 tion angles across the interfaces allow for the rays to reach these image points. This observation emphasizes that  
 572 despite the very small contact area between the rubber tire and WAAM surface, the natural as-built component  
 573 surface convexity works in the favour of the raytracing approach allowing for the WAAM internal structure to be  
 574 accessible by the ultrasound energy, even if it is generated by the corner elements. One distinct advantage of this  
 575 technique is in that it allows imaging a wider area than the coupled surface without the need to reduce the number  
 576 of contributing  $n^2$  elements and therefore utilizing the whole FMC dataset. The high acoustic mismatch between  
 577 the tire rubber (1.12 MRayls) and Ti-64 WAAM (27.49 MRayls) components leads to high refraction angles;  
 578 therefore, redirecting the sound wave towards the corners of the test piece. However, it should be noted that the  
 579 large acoustic mismatch also negatively impacts the signal amplitude transmitted into the component by increas-  
 580 ing the reflected wave energy at the interface of the rubber tire and WAAM surface.



581  
582 **Figure 16** Ray tracing from corner element number 64 to the TFM image (a) lateral pixels extending from 3  
583 mm to 40 mm below the WAAM surface, and (b) bottom pixels at the depth of 40 mm spread across the width  
584 of the Ti-64 WAAM component

## 585 6 Conclusions

### 586 6.1 Conclusion

587 This work presented, for the first time, the concept of a three-layer adaptive ultrasound TFM imaging  
588 algorithm for the inspection of WAAM components from their non-planar as-built surface, eliminating the neces-  
589 sity for a post-manufacturing surface milling. An integrated SAFT-based approach reconstructs the as-built surface  
590 and interface when deploying a customized ultrasound roller-probe. The functionality and performance of the  
591 concept approach were demonstrated on two different Ti-64 WAAM components, one with bottom drilled holes  
592 of 2 mm and 1 mm in the diameter and the other containing intentionally induced LoF defects as small as 0.5 x 5  
593 x 0.5 mm (H x W x L). The following summarizes the findings and the conclusions of this manuscript:

- 594 • Using acquired FMC data, the as-built non-planar tire/WAAM interface was reconstructed using the  
595 SAFT algorithm. Distinctive surface profiles emerging on the SAFT images allowed for the integra-  
596 tion of an automated surface finding algorithm, based on curve fitting, allowing suitable reconstruction  
597 of the WAAM surface curvature.
- 598 • The SAFT reconstruction of the as-built WAAM component was evaluated against a reference scan  
599 obtained via a non-contact metrology laser scan and the average relative error calculated as 0.04 mm.
- 600 • The ultrasonic measurement of the non-planar as-built surface geometry of the WAAM components  
601 and the time of flights of the ultrasonic rays traversing between the array and every pixel of the image  
602 was computed accommodating refractions at the two interfaces of the delay-line/rubber tire and rubber  
603 tire /WAAM sample.
- 604 • Despite the restricted contact area of only 15 mm between the rubber tire and the WAAM surface, the  
605 ray-tracing algorithm demonstrated that when using the roller-probe on WAAM walls provides thor-  
606 ough coverage of the interior volume, even when the wave is generated by corner elements.
- 607 • A fully focused image of Ti-64 WAAM components was computed and formed using the adaptive  
608 TFM algorithm with BHs and LoF defects induced at selected locations inside the WAAM compo-  
609 nents detected and imaged with SNR greater than 10dB.
- 610 • The formed TFM images of the induced LoF defects were compared to reference XCT results where  
611 strong agreement between the results was observed in terms of the defect location and extension,  
612 confirming the competency of the novel imaging approach.

613 The proposed new inspection concept and the methodology provides a new inspection alternative to im-  
614 aging of as-built WAAM components, removing the need for costly surface machining operations. The proposed  
615 methodology easily conforms to the complexities of the non-planar as-built WAAM surface and accommodates  
616 surface profile curvature in image calculations with a high degree of accuracy. The approach unlocks the potential

617 for ultrasonic phased array volumetric, or in-process multi-layer-specific, an inspection of WAAM components  
618 without the need for subsequent post-processing or machining.

### 619 6.2 Future Work

620 Future activities are to be centered around improving PAUT transduction, automated probe deployment  
621 during the WAAM build process, taking advantage of a dwell time between layers, that can allow up to minutes  
622 for inspection to be performed [60]. Alternatively, further, utilize the advantage of the high-temperature roller-  
623 probe and investigate the deployment while the torch is depositing elsewhere.

624 For the in-situ deployment, the key aim is to investigate the effect of the temperature gradients within  
625 the deposited component on ultrasonic wave propagation (velocity, refraction, and attenuation) along with the  
626 subsequent development of adaptive compensation algorithms. The velocity calibration and compensation for the  
627 anisotropic materials is to be developed, allowing for precise ray tracing within the components.

628 Lastly, the authors aim to investigate a comprehensive Probability of Detection (PoD) study focused on  
629 defect detectability and sizing in deposited WAAM components. Additionally, realizing the importance of deploy-  
630 ment within the actual WAAM build process, the PAUT probe and imaging algorithms will be further optimized  
631 for automated deployment and acquisition during the WAAM deposition process at speed.

632

633

## Acknowledgements

634 The project was supported by (I) NEWAM (EP/R027218/1), (II) EPSRC Doctoral Training Partnership  
635 (DTP) (EP/R513349/1) and (III) RoboWAAM (EP/P030165/1). We would like to thank Dr Alice Macente, for the  
636 XCT data acquisition and reconstruction, and the Scottish Funding Council's Oil and Gas Innovation Centre for  
637 funding the X-ray Computed Tomography scanner at the University of Strathclyde, owned by the Civil & Envi-  
638 ronmental Engineering

## 639 References

- 640 1. Standardization, I.O.f., *Additive Manufacturing: General: Principles: Terminology*. 2015:  
641 ISO.
- 642 2. Paolini, A., S. Kollmannsberger, and E. Rank, *Additive manufacturing in construction: a*  
643 *review on processes, applications, and digital planning methods*, *Addit. Manuf.* 30 (2019)  
644 100894. 2019.
- 645 3. Herzog, D., et al., *Additive manufacturing of metals*. Acta Materialia, 2016. **117**: p. 371-392.
- 646 4. Williams, S.W., et al., *Wire+ arc additive manufacturing*. Materials Science and Technology,  
647 2016. **32**(7): p. 641-647.
- 648 5. Martina, F., et al., *Investigation of the benefits of plasma deposition for the additive layer*  
649 *manufacture of Ti-6Al-4V*. Journal of Materials Processing Technology, 2012. **212**(6): p.  
650 1377-1386.
- 651 6. Banerjee, D. and J. Williams, *Perspectives on titanium science and technology*. Acta  
652 Materialia, 2013. **61**(3): p. 844-879.
- 653 7. Colegrove, P., et al. *System architectures for large scale wire+ arc Additive Manufacture*. in  
654 *10th International Conference on Trends in Welding Research*. 2016.
- 655 8. Xu, X., et al., *Preliminary investigation of building strategies of managing steel bulk material*  
656 *using wire+ arc additive manufacture*. Journal of Materials Engineering and Performance,  
657 2019. **28**(2): p. 594-600.
- 658 9. Xu, X., et al., *Oxide accumulation effects on wire+ arc layer-by-layer additive manufacture*  
659 *process*. Journal of Materials Processing Technology, 2018. **252**: p. 739-750.
- 660 10. Wu, B., et al., *A review of the wire arc additive manufacturing of metals: properties, defects*  
661 *and quality improvement*. Journal of Manufacturing Processes, 2018. **35**: p. 127-139.
- 662 11. Lopez, A., et al., *Non-destructive testing application of radiography and ultrasound for wire*  
663 *and arc additive manufacturing*. Additive Manufacturing, 2018. **21**: p. 298-306.
- 664 12. LEVCUN, G.A. and C.S. MAHENDRA, *Computed Radiography in the Pacific Northwest:*  
665 *Benefits, Drawbacks, and Requirements*. AMMTIAC Quarterly, 2007: p. 11-14.

- 666 13. Kourra, N., et al., *Computed tomography metrological examination of additive manufactured*  
667 *acetabular hip prosthesis cups*. Additive Manufacturing, 2018. **22**: p. 146-152.
- 668 14. Mireles, J., et al., *Analysis and correction of defects within parts fabricated using powder bed*  
669 *fusion technology*. Surface Topography: Metrology and Properties, 2015. **3**(3): p. 034002.
- 670 15. Naito, S., S. Yamamoto, and S. Yamamoto. *Novel X-ray backscatter technique for detecting*  
671 *crack below deposit*. in *7th International Conference on NDE in Relation to Structural*  
672 *Integrity for Nuclear and Pressurized Components*. 2010.
- 673 16. García-Martín, J., J. Gómez-Gil, and E. Vázquez-Sánchez, *Non-destructive techniques based*  
674 *on eddy current testing*. Sensors, 2011. **11**(3): p. 2525-2565.
- 675 17. Bento, J.B., et al., *Non-destructive testing for wire+ arc additive manufacturing of aluminium*  
676 *parts*. Additive Manufacturing, 2019. **29**: p. 100782.
- 677 18. Zhang, J., et al., *Crack path selection at the interface of wrought and wire+ arc additive*  
678 *manufactured Ti-6Al-4V*. Materials & Design, 2016. **104**: p. 365-375.
- 679 19. Du, W., et al., *Eddy current detection of subsurface defects for additive/subtractive hybrid*  
680 *manufacturing*. The International Journal of Advanced Manufacturing Technology, 2018.  
681 **95**(9): p. 3185-3195.
- 682 20. Lopez, A., et al. *Mapping of non-destructive techniques for inspection of wire and arc*  
683 *additive manufacturing*. in *Proceedings of the 7th International Conference on Mechanics*  
684 *and Materials in Design, Portugal*. 2017.
- 685 21. Javadi, Y., et al. *Intentional weld defect process: from manufacturing by robotic welding*  
686 *machine to inspection using TFM phased array*. in *AIP Conference Proceedings*. 2019. AIP  
687 Publishing LLC.
- 688 22. Willcox, M. and G. Downes, *A brief description of NDT techniques*. Toronto: NDT  
689 Equipment Limited, 2003.
- 690 23. Javadi, Y., et al., *In-process inspection of multi-pass robotic welding*. Review of Progress in  
691 Quantitative Nondestructive Evaluation, 2019.
- 692 24. Javadi, Y., et al., *Continuous monitoring of an intentionally-manufactured crack using an*  
693 *automated welding and in-process inspection system*. Materials & Design, 2020: p. 108655.
- 694 25. Pieris, D., et al., *Laser Induced Phased Arrays (LIPA) to detect nested features in additively*  
695 *manufactured components*. Materials & Design, 2020. **187**: p. 108412.
- 696 26. Zeng, Y., et al., *Laser Ultrasonic inspection of a Wire+ Arc Additive Manufactured (WAAM)*  
697 *sample with artificial defects*. Ultrasonics, 2020: p. 106273.
- 698 27. Bakre, C., M. Hassanian, and C. Lissenden. *Influence of surface roughness from additive*  
699 *manufacturing on laser ultrasonics measurements*. in *AIP Conference Proceedings*. 2019.  
700 AIP Publishing LLC.
- 701 28. Chimenti, D., *Review of air-coupled ultrasonic materials characterization*. Ultrasonics, 2014.  
702 **54**(7): p. 1804-1816.
- 703 29. Javadi, Y., et al., *Ultrasonic phased array inspection of a Wire+ Arc Additive Manufactured*  
704 *(WAAM) sample with intentionally embedded defects*. Additive Manufacturing, 2019. **29**: p.  
705 100806.
- 706 30. Lopez, A.B., et al., *Phased Array Ultrasonic Inspection of Metal Additive Manufacturing*  
707 *Parts*. Journal of Nondestructive Evaluation, 2019. **38**(3): p. 62.
- 708 31. Mohseni, E., et al. *Ultrasonic phased array inspection of wire plus arc additive manufactured*  
709 *(WAAM) titanium samples*. in *58th Annual British Conference on Non-Destructive Testing*.  
710 2019.
- 711 32. Chabot, A., et al., *Towards defect monitoring for metallic additive manufacturing components*  
712 *using phased array ultrasonic testing*. Journal of Intelligent Manufacturing, 2019: p. 1-11.
- 713 33. Chauveau, D., *Review of NDT and process monitoring techniques usable to produce high-*  
714 *quality parts by welding or additive manufacturing*. Welding in the World, 2018. **62**(5): p.  
715 1097-1118.
- 716 34. Knezović, N. and B. Dolšak, *In-process non-destructive ultrasonic testing application during*  
717 *wire plus arc additive manufacturing*. Advances in Production Engineering & Management,  
718 2018. **13**(2): p. 158-168.

- 719 35. Xiong, X., H. Zhang, and G. Wang, *Metal direct prototyping by using hybrid plasma*  
720 *deposition and milling*. Journal of Materials Processing Technology, 2009. **209**(1): p. 124-  
721 130.
- 722 36. Lockett, H., et al., *Design for Wire+ Arc Additive Manufacture: design rules and build*  
723 *orientation selection*. Journal of Engineering Design, 2017. **28**(7-9): p. 568-598.
- 724 37. Olympus-ims.com. *Ultrasonic phased array wedge for inspecting high-temperature parts up*  
725 *to 150°C*. 2020 [cited 2020 16/11/2020]; Available from: [https://www.olympus-](https://www.olympus-ims.com/en/applications/ultrasonic-phased-array-wedge-for-inspecting-high-temperature-parts-up-to-150c/#:~:text=As%20phased%20array%20probes%20heat,temperature%20of%2060%20%C2%B0C)  
726 [ims.com/en/applications/ultrasonic-phased-array-wedge-for-inspecting-high-temperature-](https://www.olympus-ims.com/en/applications/ultrasonic-phased-array-wedge-for-inspecting-high-temperature-parts-up-to-150c/#:~:text=As%20phased%20array%20probes%20heat,temperature%20of%2060%20%C2%B0C)  
727 [parts-up-to-](https://www.olympus-ims.com/en/applications/ultrasonic-phased-array-wedge-for-inspecting-high-temperature-parts-up-to-150c/#:~:text=As%20phased%20array%20probes%20heat,temperature%20of%2060%20%C2%B0C)  
728 [150c/#:~:text=As%20phased%20array%20probes%20heat,temperature%20of%2060%20%C](https://www.olympus-ims.com/en/applications/ultrasonic-phased-array-wedge-for-inspecting-high-temperature-parts-up-to-150c/#:~:text=As%20phased%20array%20probes%20heat,temperature%20of%2060%20%C2%B0C)  
729 [2%B0C](https://www.olympus-ims.com/en/applications/ultrasonic-phased-array-wedge-for-inspecting-high-temperature-parts-up-to-150c/#:~:text=As%20phased%20array%20probes%20heat,temperature%20of%2060%20%C2%B0C).
- 730 38. Hagglund, F., et al. *A novel phased array ultrasonic testing (PAUT) system for on-site*  
731 *inspection of welded joints in plastic pipes*. in *Proceedings of the 11th European Conference*  
732 *on Non-Destructive Testing (ECNDT), Prague, Czech Republic*. 2014.
- 733 39. Stratoudaki, T., et al. *Laser induced phased arrays for remote ultrasonic imaging of additive*  
734 *manufactured components*. in *57th Annual Conference of the British Institute of Non-*  
735 *Destructive Testing, NDT 2018*. 2018.
- 736 40. Lines, D., et al. *Using coded excitation to maintain signal to noise for FMC+ TFM on*  
737 *attenuating materials*. in *2019 IEEE International Ultrasonics Symposium (IUS)*. 2019. IEEE.
- 738 41. Drinkwater, B., R. Dwyer-Joyce, and P. Cawley, *A study of the transmission of ultrasound*  
739 *across solid–rubber interfaces*. The Journal of the Acoustical Society of America, 1997.  
740 **101**(2): p. 970-981.
- 741 42. Vithanage, R.K., et al., *A phased array ultrasound roller probe for automated in-*  
742 *process/interpass inspection of multipass welds*. IEEE Transactions on Industrial Electronics,  
743 2020.
- 744 43. Drinkwater, B. and P. Cawley, *AN ULTRASONIC WHEEL PROBE ALTERNATIVE TO*  
745 *LIQUID COUPLING*. 1994.
- 746 44. Mineo, C., et al. *Flexible integration of robotics, ultrasonics and metrology for the inspection*  
747 *of aerospace components*. in *AIP conference proceedings*. 2017. AIP Publishing LLC.
- 748 45. Mineo, C., et al. *Fast ultrasonic phased array inspection of complex geometries delivered*  
749 *through robotic manipulators and high speed data acquisition instrumentation*. in *2016 IEEE*  
750 *International Ultrasonics Symposium (IUS)*. 2016. IEEE.
- 751 46. Mohseni, E., et al. *A high temperature phased array ultrasonic roller probe designed for dry-*  
752 *coupled in-process inspection of wire+ arc additive manufacturing*. in *47th Annual Review of*  
753 *Progress in Quantitative Nondestructive Evaluation*. 2020.
- 754 47. Zhang, J., B.W. Drinkwater, and P.D. Wilcox, *Efficient immersion imaging of components*  
755 *with nonplanar surfaces*. IEEE transactions on ultrasonics, ferroelectrics, and frequency  
756 control, 2014. **61**(8): p. 1284-1295.
- 757 48. Holmes, C., B.W. Drinkwater, and P.D. Wilcox, *Post-processing of the full matrix of*  
758 *ultrasonic transmit–receive array data for non-destructive evaluation*. NDT & e  
759 International, 2005. **38**(8): p. 701-711.
- 760 49. Fan, C. and B.W. Drinkwater. *Comparison between beamforming and super resolution*  
761 *imaging algorithms for non-destructive evaluation*. in *AIP Conference Proceedings*. 2014.  
762 American Institute of Physics.
- 763 50. Holmes, C., B. Drinkwater, and P. Wilcox, *The post-processing of ultrasonic array data*  
764 *using the total focusing method*. Insight-Non-Destructive Testing and Condition Monitoring,  
765 2004. **46**(11): p. 677-680.
- 766 51. Han, X.-l., et al. *Application of ultrasonic phased array total focusing method in weld*  
767 *inspection using an inclined wedge*. in *Proceedings of the 2014 Symposium on*  
768 *Piezoelectricity, Acoustic Waves, and Device Applications*. 2014. IEEE.
- 769 52. Le Jeune, L., et al. *Adaptive ultrasonic imaging with the total focusing method for inspection*  
770 *of complex components immersed in water*. in *AIP Conference proceedings*. 2015. American  
771 Institute of Physics.
- 772 53. Kerr, W., S. Pierce, and P. Rowe, *Investigation of synthetic aperture methods in ultrasound*  
773 *surface imaging using elementary surface types*. Ultrasonics, 2016. **72**: p. 165-176.

- 774 54. Malkin, R.E., et al., *Surface reconstruction accuracy using ultrasonic arrays: Application to*  
775 *non-destructive testing*. NDT & E International, 2018. **96**: p. 26-34.
- 776 55. Nicolas Badeau, G.P.-A., Alain Le Duff. *Use of the Total Focusing Method with the Envelope*  
777 *Feature*. 30 March 2020 [accessed 9 April 2020]; Available from: [https://www.olympus-](https://www.olympus-ims.com/en/resources/white-papers/use-of-the-total-focusing-method-with-the-envelope-feature/)  
778 [ims.com/en/resources/white-papers/use-of-the-total-focusing-method-with-the-envelope-](https://www.olympus-ims.com/en/resources/white-papers/use-of-the-total-focusing-method-with-the-envelope-feature/)  
779 [feature/](https://www.olympus-ims.com/en/resources/white-papers/use-of-the-total-focusing-method-with-the-envelope-feature/).
- 780 56. Parrilla, M., et al. *Dynamic focusing through arbitrary geometry interfaces*. in *2008 IEEE*  
781 *Ultrasonics Symposium*. 2008. IEEE.
- 782 57. Vithanage, R.K.W., et al., *A phased array ultrasound roller probe for automated in-*  
783 *process/interpass inspection of multipass welds*. IEEE Transactions on Industrial Electronics,  
784 2020: p. 1-1.
- 785 58. *Compact laser scanner for automation & robotics*. 2021 [cited 2021 11/02]; Available from:  
786 [https://www.micro-epsilon.co.uk/2D\\_3D/laser-scanner/scanCONTROL-2600/](https://www.micro-epsilon.co.uk/2D_3D/laser-scanner/scanCONTROL-2600/).
- 787 59. Ciorau, P., J. Coulas, and T. Armit, *A contribution to length sizing of weld flaws using*  
788 *conventional, PAUT and TOFD ultrasonic techniques*. NDT. net, 2011(11).
- 789 60. Vázquez, L., et al., *Influence of interpass cooling conditions on microstructure and tensile*  
790 *properties of Ti-6Al-4V parts manufactured by WAAM*. Welding in the World, 2020. **64**: p.  
791 1377-1388.

792

793